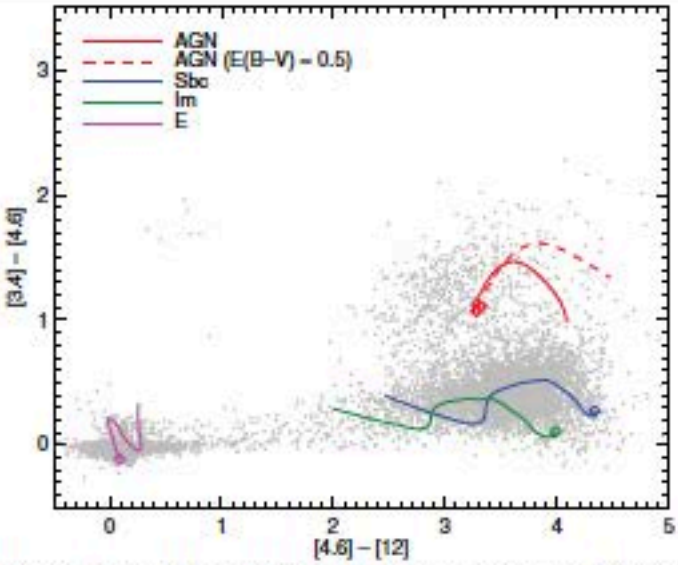

Figure 6. *WISE* band 1, 2, and 3 color–color diagram showing the distribution of objects detected by *WISE* with decl. >88°.22 which are likely dominated by external galaxies. Overlaid are tracks showing the galaxy templates of Assef et al. (2010): E (elliptical), Sbc (spiral), Im (Magellanic irregular), and AGN. Each track covers the redshift range $z = 0$ (marked with a diamond point) to $z = 1.1$, except AGNs which show $z = 0$–3.

(A color version of this figure is available in the online journal.)

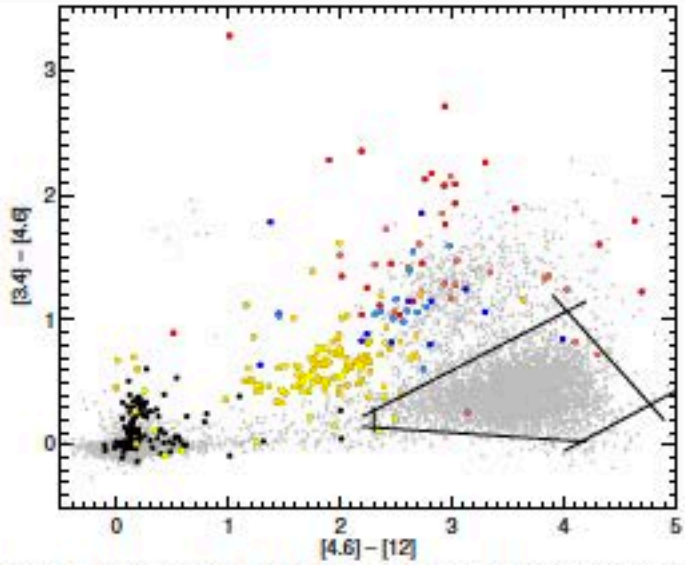

Figure 7. *WISE* band 1, 2, and 3 color–color diagram showing the distribution of diskless (black points), Class II (gold and yellow), flat SED (blue and light blue), and Class I YSOs (red and light red) from the Taurus compilation of Rebull et al. (2010) detected by *WISE*. Gray points show the location of objects detected by *WISE* with decl. >88°.22. Solid lines show the region from which we cut PAH/star-forming galaxies.

(A color version of this figure is available in the online journal.)

funded by the National Aeronautics and Space Administration (NASA); (2) the Two Micron All Sky Survey, a joint project of the University of Massachusetts and the Infrared Processing and Analysis Center (IPAC)/Caltech, funded by NASA and the National Science Foundation; (3) the SIMBAD database, operated at CDS, Strasbourg, France; and (4) the NASA/IPAC Infrared Science Archive, which is operated by JPL, Caltech, under a contract with NASA.

Facilities: Spitzer (IRAC, MIPS)

APPENDIX

We adapt the established source classification scheme of Gutermuth et al. (2008, 2009) to the *WISE* telescope wavebands. Consequently, our scheme follows the same steps. The figures included with the text in this section present objects detected by *WISE* (listed in the preliminary release catalog) from the compilation of Rebull et al. (2010). In their paper, Rebull et al. (2010) compile 215 previously identified members of the Taurus star-forming region and identify 148 new candidate members with optical, X-ray, and ultraviolet imaging. In this appendix, red, blue, and gold points mark previously known YSOs from their Table 4 (Class I, flat spectrum, and Class II), while pale red, pale blue, and yellow mark the new YSOs from their Table 5. The figures shown are used to demonstrate the context of each set of classification criteria with respect to known source types.

Our scheme is described below and is designed to be applied in the order it is written. Note that at each stage in the following scheme, objects are classified in the specified category with the given set of color and magnitude criteria and are set aside from further consideration unless specifically described in the text.

A.1. Extragalactic Object Removal

The sample of YSOs that we derive from the *WISE* data comes primarily from the matched *WISE* bands 1, 2, and 3 catalogs (3.4, 4.6, and 12 μm) that we produce for each field, requiring photometric uncertainty <0.2 mag in all three bands. The first step in extracting young stars is to remove objects from the merged catalog that are most likely to be unresolved external galaxies.

The *Spitzer* Deep, Wide-Field Survey catalog (Ashby et al. 2009) has been matched to *WISE* data for the same 8.5 deg^2 area of Boötes. We developed our criteria by plotting these data, as they will likely be dominated by external galaxies in *WISE* color space. For comparison, we also extracted *WISE* photometry from the north and south equatorial poles (decl. > +88°.22 and also decl. <−88°.22) which we assume will also consist mostly of galaxies.

In Figure 6 we plot a color–color diagram of the objects detected in the north polar field, requiring photometric error <0.2 in *WISE* bands 1, 2, and 3. For comparison, we overplot tracks showing the location of the galactic SED templates of Assef et al. (2010). Although labeled as E (elliptical), Sbc (spiral), Im (Magellanic irregular), and AGN, these templates are not built to look like specific galaxy types, but are used to model galaxies as composites of different populations. The templates are not orthogonal by design, but are intended to reproduce the typical components of galaxies: old (E), intermediate (Sbc), and young stellar populations (Im), as well as nuclear activity (AGN).

Galaxies with elevated star formation activity exhibit increased PAH-feature emission which gives them red colors in the *Spitzer* 5.8 and 8 μm bands and this property is similarly observed in the *WISE* [4.6] − [12] color. We thus label objects following *all* the constraints below as PAH/star-forming galaxies. These equations hold to delimit the region drawn in Figure 7:

$$[3.4] - [4.6] < 0.46 \times ([4.6] - [12] - 1.7)$$

$$[3.4] - [4.6] > -0.06 \times ([4.6] - [12] - 4.67)$$

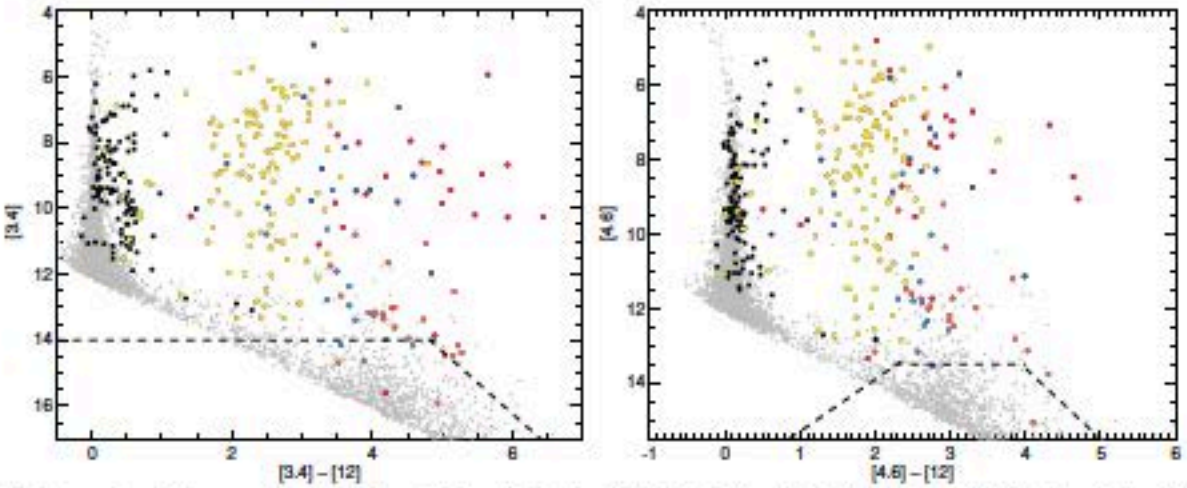

Figure 8. *WISE* color–magnitude diagrams showing diskless (black points), Class II (gold and yellow), flat SED (blue and light blue), and Class I YSOs (red and light red) from Rebull et al. (2010) detected by *WISE*. Gray points show the location of objects detected by *WISE* with decl. >−88.°22, where we have removed objects meeting the "PAH" criteria in our scheme. Dashed lines show the regions from which we cut likely AGN contaminants.

(A color version of this figure is available in the online journal.)

$$[3.4] - [4.6] < -1.0 \times ([4.6] - [12] - 5.1)$$

$$[3.4] - [4.6] > 0.48 \times ([4.6] - [12] - 4.1)$$

$$[4.6] > 12$$

$$[4.6] - [12] > 2.3.$$

Unresolved broad-line AGNs possess mid-IR colors very similar to young stars. However, on average they will be fainter than a typical young star in Galactic regions closer than ∼5 kpc, thus we use a brightness cut in *WISE* band 2 as the primary discriminant. We consider as candidate AGN those sources following either set of conditions below (see Figure 8):

$$[4.6] > 1.9 \times ([4.6] - [12] + 3.16)$$

$$[4.6] > -1.4 \times ([4.6] - [12] - 11.93)$$

$$[4.6] > 13.5$$

or

$$[3.4] > 1.9 \times ([3.4] - [12] + 2.55)$$

$$[3.4] > 14.0.$$

Both star-forming galaxies and AGNs are removed from further consideration as YSOs in the following treatment. As discussed in Gutermuth et al. (2009), Koenig et al. (2008), and Rebull et al. (2011), these criteria are imperfect as they misclassify some fraction of the extragalactic objects and also remove some fraction of true YSOs from the catalog, since faint YSOs will overlap the AGN and star-forming galaxy color/magnitude boundaries. We estimate from the Boötes field sample that 4.7 ± 0.7 galaxies deg^{-2} will appear in the YSO list as Class II sources, 2.4 ± 0.5 deg^{-2} will appear as Class I sources, and 1.8 ± 0.5 will be false transition disk objects. The north and south pole fields result in a slightly lower number of fake YSOs: the combined range of these fields, including Poisson errors, is 1.4–2.9 Class I sources, 2.2–5.4 Class II sources, and 0.9–2.7 transition disk sources per square degree.

These values are sensitive to the relative depths of *WISE* coverage (which is deeper at the poles than in the ecliptic, due to the orbit of the *WISE* telescope), any bright extended emission in the image and natural variability in the space density of stars and galaxies. For example, in the study of the wider environment around the Taurus star-forming region by Rebull et al. (2011), 724 of their 1014 YSO candidates were found to be likely contaminant galaxies, foreground or background stars, or other objects. Their sample required signal-to-noise ratio >7 in *WISE* bands 1, 2, 3, and 4, and resulted in 2.75 total fake YSOs per square degree after comparison with available spectroscopy and existing catalogs. Extrapolating this result to a *WISE* band 1, 2, and 3 sample in line with this paper, we still find only 4.8 fake YSOs per square degree. Thus, the quoted level of contamination that we present is likely an overestimate in most Galactic star-forming regions.

A.2. Shock Emission Blobs and Resolved Structure

We next remove two classes of image contaminants from the remaining catalog. As discussed by Gutermuth et al. (2009), the first are resolved shock emission knots—in *Spitzer* images these are prominent in the 4.5 μm band. The same is likely true of the *WISE* 4.6 μm band. The second class is resolved structured PAH emission; in *WISE* data, these are mainly fake detections at 12 μm due to the comparable point source-response-function of *WISE* at 12 μm and size scale of structure in the copious PAH nebulosity that is prevalent in star-forming regions.

Shock objects are those with the following colors:

$$[3.4] - [4.6] > 1.0$$

and

$$[4.6] - [12] < 2.0.$$

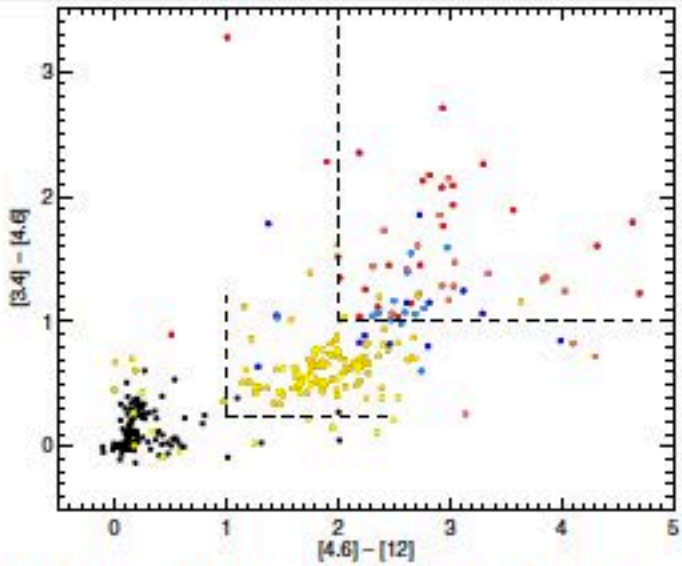

Figure 9. *WISE* band 1, 2, and 3 color–color diagram showing the distribution of diskless (black points), Class II (gold and yellow), flat SED (blue and light blue), and Class I YSOs (red and light red) from the Taurus compilation of Rebull et al. (2010) detected by *WISE*. Dashed lines indicate the boundaries by which we classify Class I and Class II sources.

(A color version of this figure is available in the online journal.)

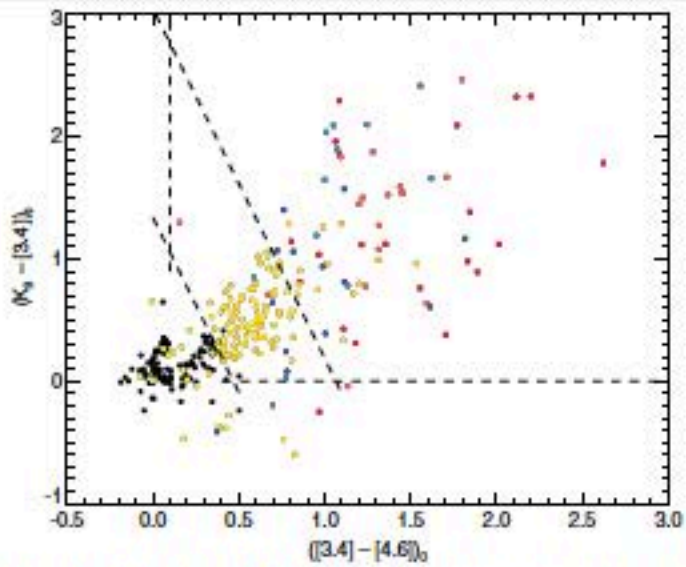

Figure 10. 2MASS K_S and *WISE* band 1 and 2 color–color diagram showing the distribution of diskless (black points), Class II (gold and yellow), flat SED (blue and light blue), and Class I YSOs (red and light red) from the Taurus compilation of Rebull et al. (2010) detected by *WISE*. Dashed lines indicate the boundaries by which we classify Class I and Class II sources.

(A color version of this figure is available in the online journal.)

Resolved PAH emission objects require either

$$[3.4] - [4.6] < 1.0$$

and

$$[4.6] - [12] > 4.9$$

or

$$[3.4] - [4.6] < 0.25$$

and

$$[4.6] - [12] > 4.75.$$

A.3. Young Stellar Objects

Having removed the previously defined contaminants, we next identify YSOs using the list of objects with good three-band *WISE* detections, i.e., those possessing photometric uncertainty <0.2 mag in *WISE* bands 1, 2, and 3. We have tested the following scheme by comparing the various color criteria with the photometry of Taurus region YSOs listed in Rebull et al. (2010) that are also detected by the *WISE* telescope. See Figure 9 for the following steps. Class I YSOs (candidate protostars) are the reddest objects, and are selected if their colors match:

$$[3.4] - [4.6] > 1.0$$

and

$$[4.6] - [12] > 2.0.$$

Class II YSOs (candidate T Tauri stars) are slightly less red objects, and are selected with colors:

$$[3.4] - [4.6] - \sigma_1 > 0.25$$

and

$$[4.6] - [12] - \sigma_2 > 1.0,$$

where

$$\sigma_1 = \sigma\,([3.4] - [4.6])$$

and

$$\sigma_2 = \sigma\,([4.6] - [12])\,,$$

where $\sigma(...)$ indicates a combined error, added in quadrature.

A.4. Using 2MASS Data

Many objects visible in *WISE* bands 1 and 2 will lack a reliable band 3 or 4 detection, due to the bright background emission present at these longer wavelengths and the drop in sensitivity. To make up for this, we match the *WISE* catalog to the 2MASS JHK_S point-source catalog (Skrutskie et al. 2006). We match using a 3″ search radius, removing objects from the 2MASS catalog with photometric quality flags D, E, F, or X in any band. This stage of the scheme requires a measurement of the intrinsic colors of objects, removing line-of-sight extinction to each source. We directly adopt the technique described by Gutermuth et al. (2005) and use the 2MASS JHK_S point-source catalog (cleaned for photometric quality as above) to generate an extinction map for each region with 36″ pixels. For each source in the merged *WISE*+2MASS source list, we take the median extinction value in a 3 × 3 pixel grid around the nearest pixel in the extinction map. Each source's *WISE*+2MASS photometry is then dereddened using the extinction law presented in Flaherty et al. (2007).

Using these dereddened colors, we find additional Class II objects requiring the following dereddened colors from the remaining unclassified objects (see Figure 10):

$$[[3.4] - [4.6]]_0 - \sigma_1 > 0.101$$

and

$$[K_S - [3.4]]_0 - \sigma_3 > 0.0$$

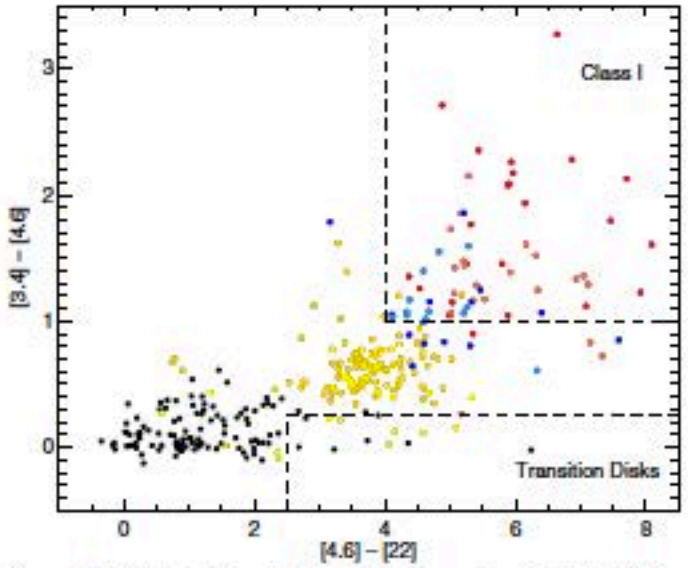

Figure 11. *WISE* band 1, 2, and 4 color–color diagram showing the distribution of diskless (black points), Class II (gold and yellow), flat SED (blue and light blue), and Class I YSOs (red and light red) from the Taurus compilation of Rebull et al. (2010) detected by *WISE*. Dashed lines indicate the boundaries by which we confirm Class I and locate transition disk candidate sources.

(A color version of this figure is available in the online journal.)

and

$$[K_S - [3.4]]_0 - \sigma_3 > -2.85714 \times ([[3.4] - [4.6]]_0 - 0.101) + 1.05$$

and

$$[3.4]_0 < 13.8,$$

where

$$\sigma_1 = \sigma\,([3.4] - [4.6])$$

$$\sigma_3 = \sigma\,(K_S - [3.4]),$$

where $\sigma(...)$ indicates a combined error, added in quadrature.

Among these new Class II objects, we classify the reddest objects as Class I objects with

$$[K_S - [3.4]]_0 - \sigma_3 > -2.85714 \times ([[3.4] - [4.6]]_0 - 0.401) + 1.9.$$

A.5. WISE Band 4 22 μm Photometry

In the same way that Gutermuth et al. (2008) used *Spitzer* MIPS 24 μm data to identify evolved so-called transition disks and confirm that Class I sources SEDs continue to rise at long wavelengths.

We first identify as "transition disks" (disks with photospheric colors between 3.4 and 12 μm but an excess at 22 μm) objects with photometric error <0.2 in *WISE* bands 1, 2, and 4 and

$$[4.6] - [22] > 2.5$$

and

$$[3.4] < 14.$$

Figure 11 shows the location of the Class I criteria specified above and the region in which we find candidate transition disk objects.

We check that previously classified Class I stars that possess photometric error <0.2 in *WISE* band 4 have rising SEDs at 22 μm. If they do not, they are considered reddened Class II sources and re-classified as such if

$$[4.6] - [22] < 4.0.$$

We also eliminate Class II stars that possess excessively blue colors. While these may possibly be stars with disks, we conservatively reject them as T Tauri stars and place them back in the unclassified pool if

$$[3.4] - [12] < -1.7 \times ([12] - [22]) + 4.3.$$

REFERENCES

Abt, H. A. 1986, ApJ, 304, 688
Alexander, R. D., & Armitage, P. J. 2009, ApJ, 704, 989
Allen, L. E., Calvet, N., D'Alessio, P., et al. 2004, ApJS, 154, 363
Allen, L. E., Myers, P. C., Di Francesco, J., et al. 2002, ApJ, 566, 993
André, P., Ward-Thompson, D., & Barsony, M. 1993, ApJ, 406, 122
Andrews, S. M., Wilner, D. J., Espaillat, C., et al. 2011, ApJ, 732, 42
Arthur, S. J., Kurtz, S. E., Franco, J., & Albarrán, M. Y. 2004, ApJ, 608, 282
Ashby, M. L. N., Stern, D., Brodwin, M., et al. 2009, ApJ, 701, 428
Assef, R. J., Kochanek, C. S., Brodwin, M., et al. 2010, ApJ, 713, 970
Bally, J., Moeckel, N., & Throop, H. 2005, in ASP Conf. Ser. 341, Chondrites and the Protoplanetary Disk, ed. A. N. Krot, E. R. D. Scott, & B. Reipurth (San Francisco, CA: ASP), 81
Barentsen, G., Vink, J. S., Drew, J. E., et al. 2011, MNRAS, 415, 103
Benjamin, R. A., Churchwell, E., Babler, B. L., et al. 2003, PASP, 115, 953
Benjamin, R. A., Whitney, B., & Churchwell, E. 2008, in ASP Conf. Ser. 381, Infrared Diagnostics of Galaxy Evolution, ed. R.-R. Chary, H. I. Teplitz, & K. Sheth (San Francisco, CA: ASP), 109
Bertoldi, F. 1989, ApJ, 346, 735
Bertoldi, F., & McKee, C. F. 1990, ApJ, 354, 529
Bonatto, C., & Bica, E. 2011, MNRAS, 414, 3769
Calvet, N., D'Alessio, P., Watson, D. M., et al. 2005, ApJ, 630, L185
Carpenter, J. M., Mamajek, E. E., Hillenbrand, L. A., & Meyer, M. R. 2006, ApJ, 651, L49
Carpenter, J. M., Snell, R. L., & Schloerb, F. P. 1995, ApJ, 450, 201
Casertano, S., & Hut, P. 1985, ApJ, 298, 80
Chabrier, G. 2003, PASP, 115, 763
Contreras, M. E., Sicilia-Aguilar, A., Muzerolle, J., et al. 2002, AJ, 124, 1585
Currie, T., Kenyon, S. J., Balog, Z., et al. 2008, ApJ, 672, 558
Dahm, S. E., & Hillenbrand, L. A. 2007, AJ, 133, 2072
Dale, J. E., & Bonnell, I. 2011, MNRAS, 414, 321
D'Alessio, P., Hartmann, L., Calvet, N., et al. 2005, ApJ, 621, 461
Dame, T. M., Hartmann, D., & Thaddeus, P. 2001, ApJ, 547, 792
Delgado, A. J., Miranda, L. F., Fernández, M., & Alfaro, E. J. 2004, AJ, 128, 330
Elmegreen, B. G. 1998, in ASP Conf. Ser. 148, Origins, ed. C. E. Woodward, J. M. Shull, & H. A. Thronson, Jr. (San Francisco, CA: ASP), 150
Elmegreen, B. G. 2000, ApJ, 530, 277
Evans, N. J., Dunham, M. M., Jørgensen, J. K., et al. 2009, ApJS, 181, 321
Flaherty, K. M., Pipher, J. L., Megeath, S. T., et al. 2007, ApJ, 663, 1069
Froebrich, D., Scholz, A., Eislöffel, J., & Murphy, G. C. 2005, A&A, 432, 575
Greene, T. P., Wilking, B. A., André, P., Young, E. T., & Lada, C. J. 1994, ApJ, 434, 614
Gritschneder, M., Burkert, A., Naab, T., & Walch, S. 2010, ApJ, 723, 971
Guetter, H. H., & Turner, D. G. 1997, AJ, 113, 2116
Gutermuth, R. A., Megeath, S. T., Muzerolle, J., et al. 2004, ApJS, 154, 374
Gutermuth, R. A., Megeath, S. T., Myers, P. C., et al. 2009, ApJS, 184, 18
Gutermuth, R. A., Megeath, S. T., Pipher, J. L., et al. 2005, ApJ, 632, 397
Gutermuth, R. A., Myers, P. C., Megeath, S. T., et al. 2008, ApJ, 674, 336
Haikala, L. K. 1995, A&A, 294, 89
Haisch, K. E., Jr., Lada, E. A., & Lada, C. J. 2001, ApJ, 553, L153
Hartmann, L., Megeath, S. T., Allen, L., et al. 2005, ApJ, 629, 881
Heiderman, A., Evans, N. J., II, Allen, L. E., Huard, T., & Heyer, M. 2010, ApJ, 723, 1019
Hernández, J., Briceño, C., Calvet, N., et al. 2006, ApJ, 652, 472
Hernández, J., Hartmann, L., Calvet, N., et al. 2008, ApJ, 686, 1195
Hester, J. J., Scowen, P. A., Sankrit, R., et al. 1996, AJ, 111, 2349
Hillwig, T. C., Gies, D. R., Bagnuolo, W. G., Jr., et al. 2006, ApJ, 639, 1069